Indian Journal of Pure & Applied Physics
Vol. 60, January 2022, pp. 59-71

Structural, dielectric and ac electrical properties of nano-structured $Mn_{0.6}Co_{0.2}Ni_{0.2}Fe_2O_4$ ternary ferrite synthesized by citrate-gel auto-combustion technique

Laxmi J Hathiya*, J D Baraliya, H O Jethva & H H Joshi
Department of Physics, Saurashtra University, Rajkot, Gujarat-360 005, India

Received 9 September 2021; accepted 23 November 2021

The present paper reports the structural, dielectric and ac electrical properties of nanoparticles of mixed polycrystalline spinel ferrite ternary compound $Mn_{0.6}Co_{0.2}Ni_{0.2}Fe_2O_4$ synthesized by using the citrate-gel auto-combustion technique. The standard characterization techniques such as EDAX, XRD and FTIR were primarily employed to confirm the elemental stoichiometry, crystallized single-phase, IR-functional groups. These measurements ascertained the formation of monophasic and pure ferrite compound. The powder X-ray diffraction analysis was done to determine the lattice constant(0.8420 nm), crystallite size(21 nm), X-ray density (5.16 g/cm^3), distribution of cations among the tetrahedral and octahedral sites of spinel lattice(with iron-Fe^{3+} distribution ratio among A and B sites is 0.25), bond angles and bond lengths. The theoretical lattice constant is found to be 0.8422 nm. The nature and position of the IR-bands were observed through FTIR spectroscopy. The high-frequency band v_1 (A-site vibrations) lies at 563.07 cm^{-1} while the low-frequency band v_2 (B-site vibrations) lies at 462.59 cm^{-1} . The force constants for the tetrahedral site (k_t) and octahedral site (k_o) were deduced 1.33×10^2 N/m and 1.27×10^2 N/m, respectively. Frequency dependence of dielectric constant and tangent loss has been explained by the Maxwell Wagner model and Koop's theory. The Jonscher's power low was used to describe the ac conductivity measurements. The Nyquist and cole-cole plots indicated presence of grain contribution in the conduction mechanism.

Keywords: Nano ferrite; Auto-combustion; XRD; FTIR; Dielectric; Cole-cole plot

1 Introduction

Spinel ferrites are the most important magnetic oxides having *fcc* structure formed by the oxygen ions which contain the metallic cations residing at either tetrahedral (A) or octahedral [B] site. They have the general formula AB_2O_4, where A and B represent the tetrahedral site and octahedral site, respectively. The spinel unit cell has 32 B-sites and 64 A-sites accessible to cations out of which 24 B and 8 A sites are engaged by cations. Spinel ferrites raised as a novel group of nanomaterials because of their interesting magnetic[1], electrical[2] and optical[3] properties and therefore they are used in many applications like magnetic recording[4], as photocatalyst[5] and as antibacterial agents[6]. The magnetic, electric and dielectric characteristics of spinel ferrites conclusively depend upon the structural properties and for that, the non-destructive characterization techniques like X-ray diffraction and infrared spectroscopy are especially suited for such investigations[7]. The distribution of cations in spinel lattice is different in ferrite nano-particles compared to their micron-size coarse grained ferrite counterpart[8]. This gives rise to interesting magnetic and electrical properties of nano-structured ferrites.

The structural and electrical properties can be modified when the particle size of a material is reduced[9]. Generally, substitutions of divalent or trivalent ions in pure ferrites result in the modification of their structural, electrical and magnetic properties[10]. The spinel ferrites having a transition metal as divalent cation like $MnFe_2O_4$ have attracted the attention of researchers because of their exciting properties like excellent chemical stability, high saturation magnetization & environment friendly[11,12] and well known for their specialised applications[13-15]. With the property of greatest physical and chemical stability, $CoFe_2O_4$ nanoparticles are useful in high density information recording, ferrofluids, storage systems and biological applications[16-19]. Nickel ferrite ($NiFe_2O_4$) is one of the important soft ferrite materials with spinel structure because of its typical ferromagnetic property and high electrical resistivity[20-22]. It has been reported that the electrical conductivity and the dielectric loss decrease with the reduction of grain size in nano-structured nickel ferrites[23-24]. These remarkable electrical and magnetic properties depend upon the

*Corresponding author: (E-mail: laxmihathiya864@gmail.com)

nature of the ions, their charges and their distribution among tetrahedral (A) and octahedral (B) sites[25]. The Mn^{2+} substituted ferrites exhibit interesting physical properties and Mn^{2+} has strong preference for tetrahedral (A) site. Moreover, $CoFe_2O_4$ is a partially inverse spinel having degree of inversion sensitive to thermal history of the specimen and Co^{2+} ion introduces a uniaxial anisotropy in the material due to more spin-orbit coupling than other 3d transition metal ions and its effect is more pronounced when it occupies the octahedral site[26]. The $NiFe_2O_4$ is an inverse spinel ferrite.

Therefore, the idea of preparing nano-structured ternary ferrite composition having transition divalent metals (Mn, Co, Ni) was conceived to obtain ferrite material with improved physical and functional properties. The motivation for selecting the present compound is twofold, first, to synthesize the ternary ferrite nano-particles by auto-combustion technique and second, to study the effect of cation distribution affecting the structural and electrical properties in nano-regime.

It is well known that the method of synthesis of nano ferrite particles plays a key role with regard to their structural and physical properties[27]. Among various available wet-chemical routes, the auto-combustion technique is very popular and precise technique for preparation of pure and uniform ferrite nano-particles[28-31].

The present work aims to study the structural, dielectric and ac electrical properties of ternary nano-structured ferrite $Mn_{0.6}Co_{0.2}Ni_{0.2}Fe_2O_4$ prepared by citrate-gel auto combustion technique as no information exists in the literature on such ternary nano-structured ferrite compound.

2 Experimental

2.1 Synthesis process

$Mn_{0.6}Co_{0.2}Ni_{0.2}Fe_2O_4$ nano ferrite was synthesized by citrate-gel auto combustion technique using the EMSURE® ACS, ISO reagent Ph Eur. (99%) grade chemicals by Merck, Germany, manganese nitrate $Mn(NO_3)_2.4H_2O$, cobalt nitrate $Co(NO_3)_2.6H_2O$, nickel nitrate $Ni(NO_3)_2.6H_2O$, ferric nitrate $Fe(NO_3)_3.9H_2O$, citric acid $C_6H_8O_7.H_2O$ and ammonia solution NH_3 (25%).

Calculated quantities of divalent metal nitrate salts and ferric nitrate salt were dissolved in double distilled water and the required amount of aqueous citric acid solution was added as a coordinating agent in a molar ratio of divalent nitrate, ferric nitrate to citric acid 1:2:1. Ammonia solution was added to this nitrate-citrate mixture to adjust the pH of the solution to 7. This mixture was heated on a hot plate with magnetic stirring at about 100 °C for 1 hour to obtain a highly viscous gel. The resultant gel was further heated at a temperature of 200 °C for 1 hour which triggers a fast flameless auto-combustion reaction as shown in Fig. 1. After the combustion process, grey-colored fluffy ferrite material shaped like a branched

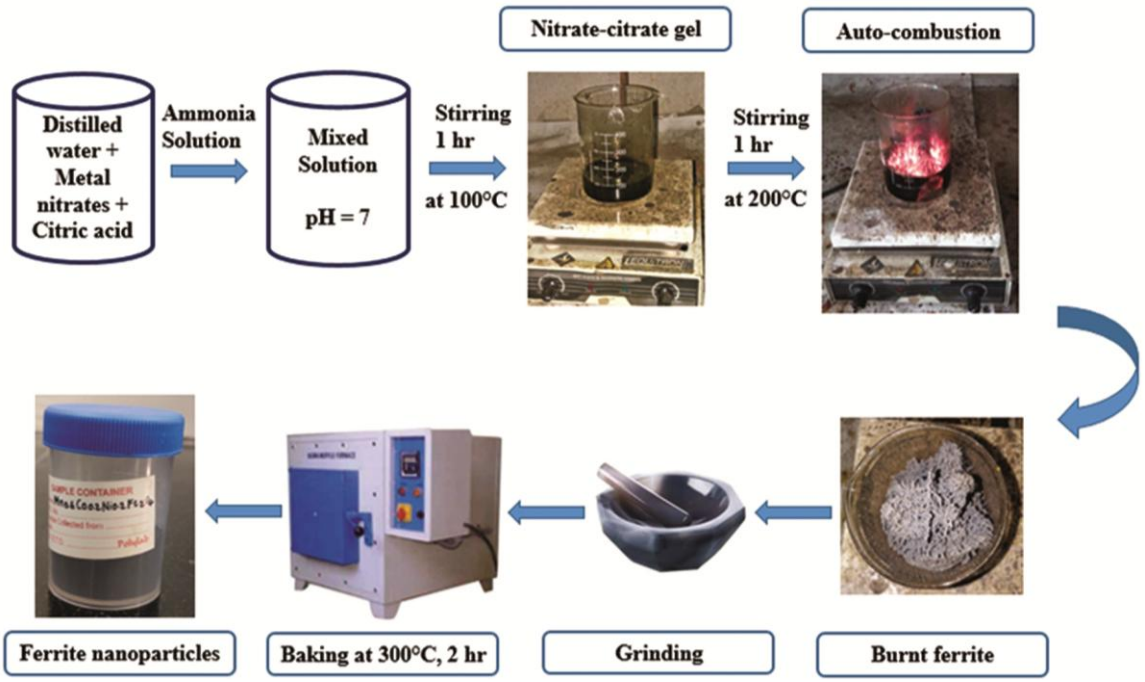

Fig. 1 — Synthesis process of nanocrystalline $Mn_{0.6}Co_{0.2}Ni_{0.2}Fe_2O_4$.

tree was generated. This product was ground and baked at 300 °C for 2 hours in a muffle furnace. To study the dielectric and ac electrical measurements a pellet of diameter 10 mm and thickness 1 mm was prepared under the pressure of 5 ton/in^2 using a hydraulic press.

2.2 Characterization techniques

The compositional stoichiometry of the final ferrite product was ascertained by energy dispersive analysis of X-rays (EDAX) mapping using Philips make ESEM EDAX XL-30. The structural characterization of the synthesized sample was carried out by Phillips X-ray diffractometer (PW 3040/60, X'pert PRO) using Cu Kα radiation *(λ=1.5405Å)* at room temperature by continuous scanning in the range of 10 to 80 θº. The Nicolet 1510 FT-IR spectrometer was used to carry out the infrared spectroscopic measurements in the KBr medium at room temperature. The dielectric and ac electrical measurements were recorded in the frequency range of 100 Hz to 1 MHz by Agilent 4284A LCR meter at room temperature.

3 Results and discussion

3.1 Structural properties

3.1.1 EDAX study

The EDAX pattern of $Mn_{0.6}Co_{0.2}Ni_{0.2}Fe_2O_4$ is shown in Fig. 2 and the results of elemental analysis are given in Table 1 showing excellent confirmation of the expected compositional stoichiometry.

Table 1 shows that all the initial materials must have fully undergone the chemical reaction to form the expected ferrite composition without loss of any ingredient. No trace of any impurity was found indicating the purity of the synthesized nano-structured ferrite sample.

3.1.2 XRD analysis

The X-ray diffractogram of the sample is shown in Fig. 3 which confirmed the formation of a well-defined single-phase cubic spinel structure belonging to the *Fd3m* space group already reported by the authors[32].

All the Bragg reflections were indexed using PowderX software. The strongest reflection from the (311) plane with the fundamental reflections from the crystal planes are (111), (220), (222), (400), (422), (333), (440) and (533) indicates the *fcc* crystal structure of the spinel ferrite. However, the unindexed

Table 1 — EDAX elemental analysis of $Mn_{0.6}Co_{0.2}Ni_{0.2}Fe_2O_4$

Element	Atomic (%)		Weight (%)	
	Expected	EDAX	Expected	EDAX
Mn	8.57	8.56	14.19	14.18
Co	2.86	2.83	5.08	5.04
Ni	2.86	2.85	5.06	5.02
Fe	28.57	28.60	48.11	48.38
O	57.14	57.16	27.56	27.38
Total	100	-	100	-

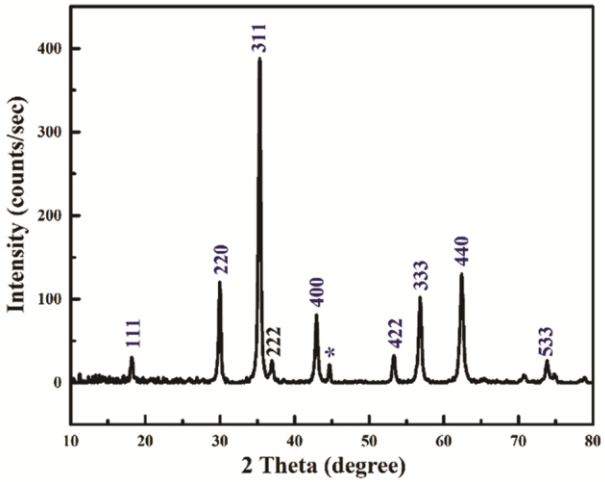

Fig. 3 — XRD pattern of $Mn_{0.6}Co_{0.2}Ni_{0.2}Fe_2O_4$.

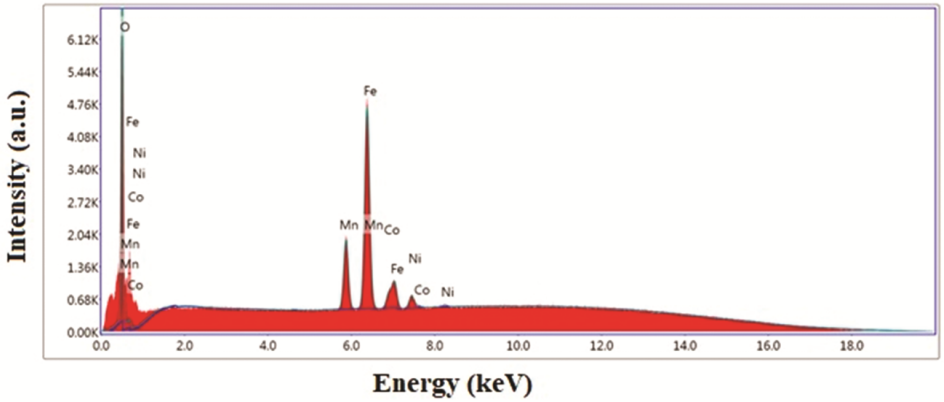

Fig. 2 — EDAX pattern of $Mn_{0.6}Co_{0.2}Ni_{0.2}Fe_2O_4$.

Bragg reflection marked by '*' is due to the presence of a slender amount of Co_3Fe_7 in the sample[32]. The average crystallite size (D) was calculated from the most intense peak (311) by using the Debye-Scherer formula:

$$D = \frac{k\lambda}{\beta cos\theta} \quad \ldots (1)$$

where, λ is the wavelength (1.5405Å), θ is the Bragg's angle, β is the full width at half maximum (FWHM) in radian and k is a constant approximately equal to 0.9.

The X-ray density ($\rho_{X\text{-}ray}$) was calculated by

$$\rho_{X\text{-}ray} = \frac{8M_W}{N_A a^3} \quad \ldots (2)$$

where, M_W is the molecular weight of the ferrite sample = 232.18 g/mol, N_A is the Avogadro's number and a is the experimental lattice constant.

The bulk density (ρ_{bulk}) of the sample was calculated according to the relation

$$\rho_{bulk} = \frac{m}{\pi r^2 t} \quad \ldots (3)$$

where, m is the mass of the pellet, t and r are the thickness and radius of the pellet, respectively.

The porosity (P) of the sample pellet was calculated according to the following equation

$$P = \frac{\rho_{X-ray} - \rho_{bulk}}{\rho_{X-ray}} \times 100 \quad \ldots (4)$$

The surface area (S) was calculated using the following formula

$$S = \frac{6000}{\rho_{X-ray}\, D} \quad \ldots (5)$$

Various structural parameters obtained from XRD analysis (Table 2) are in conformity with the reported data for pristine undoped parent ferrite $MnFe_2O_4$[33,34]. As appears from the structure factors given in Table 3, the Bragg reflections (220), (422), (400) and (440) are the most sensitive to the distribution of cations among tetrahedral (A) and octahedral [B] sites of the spinel lattice[35], hence, the cation distribution can be estimated by comparing the experimental and calculated XRD Bragg peaks intensity ratios I(440)/I(422) and I(220)/I(400)[36]. The calculated and observed intensity ratios were compared for various combinations of cation distributions[37] and final best match values are given in Table 3.

According to site preference energy values[38] for individual cations in $Mn_{0.6}Co_{0.2}Ni_{0.2}Fe_2O_4$, the cations Ni^{2+} and Co^{2+} occupy only B-site whereas Mn^{2+} has marked preference for A-site[39]. This determines the occupancy of Fe^{3+} ions among A- and B-sites. Any alteration in the distribution of cations causes a significant change in the theoretical values of X-ray diffraction intensity ratios[40]. Therefore, to reach the final cation distribution, the site occupancy of all the cations was varied for various combinations and the distribution of cations for the present composition was concluded as shown in Table 3. The ionic radius of the tetrahedral and octahedral sites r_A and r_B, respectively were calculated by[41],

$$r_A = C_{AMn}{}^{2+} r(Mn^{2+}) + C_{AFe}{}^{3+} r(Fe^{3+}) \quad \ldots (6)$$

$$r_B = \frac{1}{2}\left[C_{BNi}{}^{2+} r(Ni^{2+}) + C_{BCo}{}^{2+} r(Co^{2+}) + C_{BFe}{}^{3+} r(Fe^{3+})\right] \quad \ldots (7)$$

where, $r(Mn^{2+})$, $r(Ni^{2+})$, $r(Co^{2+})$ and $r(Fe^{3+})$ are the ionic radii of Mn^{2+} (0.80 Å), Ni^{2+} (0.69 Å), Co^{2+} (0.72 Å) and Fe^{3+} (0.64 Å), respectively, while C_{AMn} and C_{AFe} are the concentrations of the Mn^{2+} and Fe^{3+} ions on A-site and C_{BNi}, C_{BCo} and C_{BFe} are the concentrations of the Ni^{2+}, Co^{2+} and Fe^{3+} ions on B-site.

As there is a correlation between the ionic radii and the lattice constant, the lattice constant (a_{th}) was calculated theoretically using the relation suggested[42] as follows,

$$a_{th} = \frac{8}{3\sqrt{3}}\left[(r_A + R_o) + \sqrt{3}\,(r_B + R_o)\right] \quad \ldots (8)$$

where, R_o is the radius of the oxygen ion (1.32Å)

The value of a_{th} is in good agreement with the experimental value a_{exp} obtained from X-ray diffraction (Table 4). From the following relations, the hopping length (distance between magnetic ions) for the tetrahedral and octahedral site is determined:

Table 2 — Various structural parameters obtained from XRD analysis

Lattice Parameter a_{exp} (nm)	0.8420
Crystallite size D_{XRD} (nm)	21.00
Unit Cell Volume V_{cell} $(nm)^3$	0.5969
X-Ray Density ρ_{XRD} (g/cm^3)	5.16
Bulk density ρ_{bulk} (g/cm^3)	2.06
Porosity P (%)	60.07
Surface area S (cm^3/g)	5.5×10^6

Table 3 — Comparison of intensity ratios and obtained cation distribution

(hkl)	Structure factor	Intensity ratio	Obs.	Cal.
(440)	$8(b_A + 2b_B + 4b_O)$	I(440)/I(422)	2.47	2.47
(422)	$8b_A$			
(220)	$-8b_A$	I(220)/I(400)	1.49	1.48
(400)	$8(-b_A + 2b_B + 4b_O)$			
Cation distribution		$(Mn_{0.6}Fe_{0.4})^A\,[Ni_{0.2}Co_{0.2}Fe_{1.6}]^B\,O_4$		

Table 4 — Calculated parameters deduced from XRD analysis

Molecular weight of A-site M_1 (kg) × 10^{-3}	55.30
Molecular weight of B-site M_2 (kg) × 10^{-3}	112.31
Ionic radii r_A (nm)	0.0736
Ionic radii r_B (nm)	0.0653
Lattice parameter a_{th} (nm)	0.8422
Hopping length L_A (nm)	0.365
Hopping length L_B (nm)	0.298
Oxygen positional parameter u^{3m} (nm)	0.0266
Oxygen positional parameter u^{43m} (nm)	0.0391
Tetrahedral site radii R_A (nm)	0.0751
Octahedral site radii R_B (nm)	0.0642
Tetrahedral bond length d_{AX} (nm)	0.2062
Octahedral bond length d_{BX} (nm)	0.1976
Shared tetrahedral edge length d_{AEX} (nm)	0.3367
Shared octahedral edge length d_{BEX} (nm)	0.2586
Unshared octahedral edge length d_{BEUX} (nm)	0.2984

Hopping length for tetrahedral site (L_A),

$$L_A = \frac{a\sqrt{3}}{4} \quad \ldots (9)$$

Hopping length for octahedral site (L_B),

$$L_B = \frac{a\sqrt{2}}{4} \quad \ldots (10)$$

The oxygen positional parameter or anion parameter (u), which is the distance between the oxygen ion and the face of the cube edge along the cube diagonal of the spinel lattice for octahedral site u^{3m} and tetrahedral site u^{43m} were calculated as follows:

For the unit-cell origin at *3m* on the octahedral site

$$u^{3m} = \frac{\frac{1}{4}R^2 - \frac{2}{3} + \left(\frac{11}{48}R^2 - \frac{1}{18}\right)^{\frac{1}{2}}}{2R^2 - 2} \quad \ldots (11)$$

If the oxygen parameter u^{3m} is exactly 0.025 nm, the oxygen ions form a cubic close packed array otherwise there is a departure from ideal value because of presence of cations.

Assuming hard sphere model, for the unit-cell origin at *43m* on the tetrahedral site

$$u^{43m} = \frac{\frac{1}{2}R^2 - \frac{11}{12} + \left(\frac{11}{48}R^2 - \frac{1}{18}\right)^{\frac{1}{2}}}{2R^2 - 2} \quad \ldots (12)$$

where $R = \frac{B-O}{A-O}$,

The bond lengths $A-O$ *and* $B-O$ were calculated based on the cation distribution; $A-O =< r_A + r(O^{2-}) >$ and $B-O =< r_B + r(O^{2-}) >$.

For a perfect *fcc* structure, the ideal oxygen positional parameter (u_{ideal}) for *3m* and *43m* are $u_{ideal}^{3m} = 0.250$ Å and $u_{ideal}^{43m} = 0.375$ Å and the values of the present ferrite sample are in accordance with these values.

$$R_A = (u^{43m} - 0.25)\, a\sqrt{3} - R_o$$
$$R_B = (0.625 - u^{43m})\, a - R_o \quad \ldots (13)$$

The values of site radii R_A and R_B are compared with the ionic radii r_A and r_B (Table 4) and a comparison of experimental lattice constant (a_{exp}) with the calculated one a_{th} show good agreement. The value of oxygen parameter (u^{3m}) greater than 0.025 nm implies the expansion of oxygen lattice around A-site and corresponding contraction around B-sites. The symmetry around A-site is strictly cubic even if (u^{3m}) is not equal to 0.025 nm, because even after the displacement along three body diagonals of oxygen anions they still form tetrahedral.

Using the value of 'a_{exp}' and by assuming the centre of symmetry at (3/8, 3/8, 3/8) for which the positional parameter u^{43m} is used to calculate the following parameters:

$$d_{AX} = a\sqrt{3}\left(u - \tfrac{1}{4}\right) \text{ Tetrahedral bond length}$$
$$d_{BX} = a\left[3u^2 - \left(\tfrac{11}{4}\right)u + \left(\tfrac{43}{64}\right)\right]^{\frac{1}{2}} \text{ Octahedral bond length}$$
$$d_{AEX} = a\sqrt{2}\left(2u - \tfrac{1}{2}\right) \text{ Shared tetrahedral edge length}$$
$$d_{BEX} = a\sqrt{2}(1 - 2u) \text{ Shared octahedral edge length}$$
$$d_{BEXU} = a\left[4u^2 - 3u + \left(\tfrac{11}{16}\right)\right]^{\frac{1}{2}} \text{ Unshared octahedral edge length} \quad \ldots (14)$$

The calculated parameters deduced from XRD analysis are given in Table 4.

It is well known that the magnitude of super-exchange interactions is directly proportional to the bond angles and inversely proportional to the bond lengths so these parameters provide useful information about the interactions present within the system[43].

Figure 4 shows the interionic distances and bond angles between ions of spinel ferrites. The interionic distances between the cations *Me – Me* (*b, c, d, e, f*) and between the cation and anion *Me – O* (*p, q, r, s*) were calculated using the experimental values of lattice constant (*a*) and oxygen positional parameters (u^{3m}) by the following relations which are given in Table 5.

$$M_e - O \quad M_e - M_e$$
$$p = a\left(\tfrac{1}{2} - u^{3m}\right) \quad b = \left(\tfrac{a}{4}\right)2^{\frac{1}{2}}$$
$$q = a\left(u^{3m} - \tfrac{1}{8}\right)3^{\frac{1}{2}} \quad c = \left(\tfrac{a}{8}\right)11^{\frac{1}{2}}$$
$$r = a\left(u^{3m} - \tfrac{1}{8}\right)11^{\frac{1}{2}} \quad d = \left(\tfrac{a}{4}\right)3^{\frac{1}{2}}$$
$$s = \tfrac{a}{3}\left(u^{3m} + \tfrac{1}{2}\right)3^{\frac{1}{2}} \quad e = \left(\tfrac{3a}{8}\right)3^{\frac{1}{2}}$$

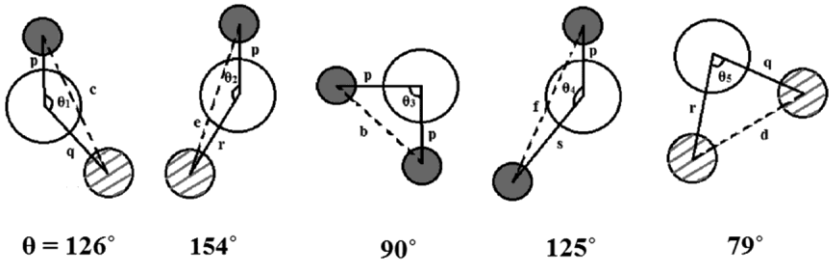

Fig. 4 — Interionic distances and bond angles.

Table 5 — Interionic distances (nm) and bond angles (degree)

b	0.2976
c	0.3490
d	0.3645
e	0.5468
f	0.5155
p	0.1967
q	0.2062
r	0.3949
s	0.3725
θ_1	120.07
θ_2	132.25
θ_3	98.41
θ_4	127.09
θ_5	66.25

$$f = \frac{a}{4}\Big) 6^{\frac{1}{2}} \quad \ldots (15)$$

The bond angles (θ_1, θ_2, θ_3, θ_4, θ_5) were calculated by simple trigonometric principle using the interionic distances with the help of the equations:

$$\theta_1 = \cos^{-1}\left[\frac{p^2+q^2-c^2}{2pq}\right.$$
$$\theta_2 = \cos^{-1}\left[\frac{p^2+r^2-e^2}{2pr}\right.$$
$$\theta_3 = \cos^{-1}\left[\frac{2p^2-b^2}{2p^2}\right.$$
$$\theta_4 = \cos^{-1}\left[\frac{p^2+s^2-f^2}{2ps}\right.$$
$$\theta_5 = \cos^{-1}\left[\frac{r^2+q^2-d^2}{2rq}\right. \quad \ldots (16)$$

The obtained values of interionic distance and bond angles(Table 5) are in conformity with the values of spinel ferrites. There are basically three types of super-exchange interactions to operate in the spinels : (i) Inter-sublattice exchange interaction, J_{AB} , interaction between cations on A and B sublattices (ii) Intra-sublattice interactions, J_{BB} and J_{AA} , interactions operating among the cations on A sites and B sites. Fig. 4 gives the possible M_e-*O*-M_e (where *M = A or B*) configurations involving these exchange interactions. The hatched circles represent the A-site cations and small dark circles represent B-site cations. Among AB configurations, only '*pqc*' configuration is favourable since the *M-O* distance as well as angle *M-O-M* (126°) are favourable for having strong exchange integration. The other AB configuration like '*pre*' has favourable angle (154°) but due to large *M-O* distance reasonable exchange interaction cannot be expected. Among BB interactions, the *M-O* distance is small for '*ppb*' configuration but angle (90°) is unfavourable. For other BB configurations the angles and distances both are unfavourable. Thus, overall BB super-exchange interactions are expected to stay lower in strength as compared to the AB super-exchange interactions. Among AA interactions, only one '*rqd*' configuration is shown having both the *M-O* distances much larger than any AB or BB distance. Since B-cations direct their T_{2g} orbital towards each other, which not the case for AA interaction, the AA interaction is expected to be the weakest of all the super-exchange interactions. In general, for spinel structure, the relative strengths of exchange interactions are given as: $|J_{AB}| >> |J_{BB}| > |J_{AA}|$.

3.2 FTIR study

The FTIR spectrum was recorded at 300K in the wavenumber range of 4000-400 cm^{-1} as shown in Fig. 5. The infrared absorption bands v_1 and v_2 corresponding to tetrahedral (A) and octahedral [B] sites, respectively were found around 600 cm^{-1} and 400 cm^{-1}, which is the basic characteristic of spinel ferrite.

The infrared absorption band v_1 is caused by the tetrahedral metal-oxygen $Fe^{3+}-O^{2-}$ stretching vibrations and the band v_2 is caused by the octahedral metal-oxygen $Fe^{3+}-O^{2-}$ bending vibrations in the octahedral site[44,45]. The high-frequency band v_1 lies at 563.07 cm^{-1} while the low-frequency band v_2 lies at 462.59 cm^{-1}. Several bands present in the IR spectrum are corresponding to the characteristic IR-functional groups and bonds present in the as-prepared ferrite composition. The appearance of the sharp band at 1112 cm^{-1} is a consequence of the out-of-plane bending vibrations of *O–H* stretching of the absorbed

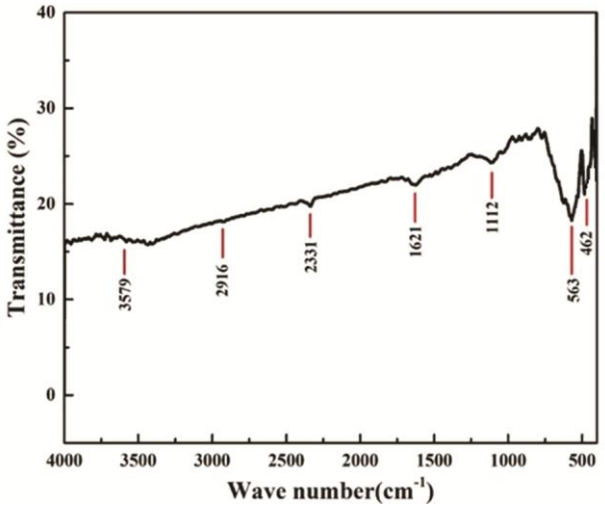

Fig. 5 — FTIR Spectrum of $Mn_{0.6}Co_{0.2}Ni_{0.2}Fe_2O_4$.

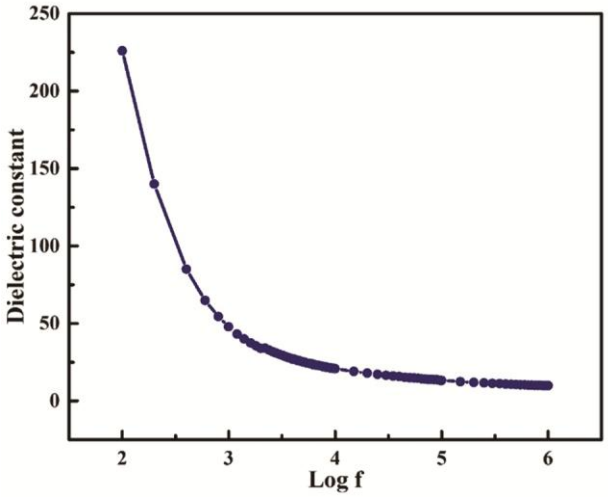

Fig. 6 — Frequency dependence of dielectric constant for $Mn_{0.6}Co_{0.2}Ni_{0.2}Fe_2O_4$.

water molecules[46]. The band at 1621 cm^{-1} corresponds to stretching and bending vibrations of the *H–O–H* bond which suggests the physical adsorption of H_2O on the surfaces[47,48]. The presence of a band at 2331 cm^{-1} is significant of adsorbed or atmospheric CO_2 and the presence of a low-intensity band at 3579 cm^{-1} is assigned to the stretching vibrations of the absorbed water on the surface of the sample[49]. A very slight band around 2916 cm^{-1} is attributed because of hydrogen bonding[50]. The force constants for the tetrahedral site (k_t) and octahedral site (k_o) were obtained 1.33×10^2 N/m and 1.27×10^2 N/m, respectively in terms of molecular weight of cations on respective site and absorption band position, using Waldron's method in simplified form, are given by[51]:

$$k_t = 7.62 \times M_1 \times \nu_1^2 \times 10^{-7}$$

$$k_o = 10.62 \times \frac{M_2}{2} \times \nu_2^2 \times 10^{-7} \quad \ldots (17)$$

where, M_1 and M_2 are the molecular weight of cations on tetrahedral and octahedral sites, respectively calculated from cation distribution.

3.3 Dielectric properties

The dielectric studies are very important in order to investigate the internal features and microstructure of electro-ceramic material, which may be affected by various parameters such as variation of elemental composition, particle size, electric field, operating temperature and frequency, etc. There are two important parameters of dielectric material, namely, dielectric constant and dielectric loss. In the present investigation, the frequency dependence of both dielectric constant and dielectric loss is studied for $Mn_{0.6}Co_{0.2}Ni_{0.2}Fe_2O_4$ at room temperature.

The dielectric constant value for the sample was calculated by using the equation:

$$\varepsilon' = \frac{Cd}{\varepsilon_0 A} \quad \ldots (18)$$

where, C is the capacitance in Farad, d is the thickness of the pellet in meter, A is the cross-sectional area of the pellet in $meter^2$, and ε_0 is the permittivity of free space.

Figure 6 shows that as frequency increases the value of dielectric constant initially decreases and then it becomes constant at higher values of frequency. Such type of behaviour of ferrites is reported in the literature[52,53], which is in agreement with the Koops and Maxwell-Wagner models[54-56]. On the basis of these models, behaviour of dielectric constant at low frequencies can be assigned to the presence of all four types polarizations in the sample, which are electronic, ionic, dipolar and space-charge polarization, while the same at higher frequencies indicates inadequacy of electric dipoles to follow the change in frequencies of applied changing electric field[52,57]. As per the reports available in the literature[52,58,59], in ferrites, the process of electric conduction and dielectric polarization can be assigned to the electron and hole exchange between ions which have occupied the interstitial lattice sites. As the frequency increases, the exchange process of electron and hole between the ions is unable to follow the applied changing electric field. This unability results into fall off the polarization and hence dielectric constant remains unchanged.

It is observed from the Fig. 7 that dielectric loss is exhibiting the high value at low frequency, but found

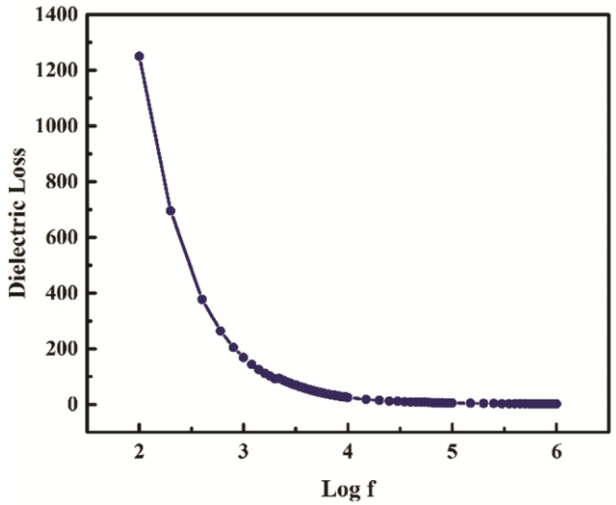

Fig. 7 — Frequency dependence of dielectric loss.

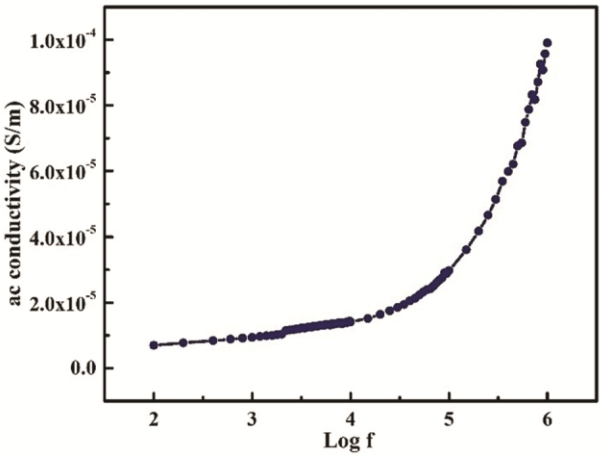

Fig. 8 — Frequency dependence ac conductivity.

gradually decreased as frequency is increased and it becomes constant at higher frequencies. This behavior is similar to that of the dielectric constant and can be explained in similar way as in the case of the dielectric constant. Generally, the frequency response of dielectric loss shows a small relaxation peak at higher frequencies when the frequency of an externally applied ac field becomes equal to the natural frequency of the oscillating system, resulting in the transfer of maximum energy to the oscillating system, due to which resonance is set up[52,53]. In the present case, the absence of such relaxation peak may be due to the relatively high resistivity of the sample or may be the lower value of maximum frequency used in the present study[52].

3.4 AC electrical properties

3.4.1 AC conductivity mechanism

The formula used to calculate ac conductivity was $\sigma_{ac} = \omega\varepsilon_o\varepsilon''$ [60], where the symbols have their usual meaning.

The ac conductivity curve (Fig. 8) shows two different regions; a low frequency plateau region in which conductivity is frequency independent up to certain value of applied frequency and a high frequency dispersion region in which conductivity shows fully dependency on applied frequency. The frequency independent conductivity can be treated as dc conductivity of the sample, the value of which can be calculated from the plot by taking the intersect on the Y axis[61]. The dc conductivity can be attribute to the drift mobility of the charge carriers[52]. This is the region in which transportation of the ions occurs on an infinite path[62], which results into much faster travel and jumping of the ions from one site to another site. The successful jump of the ions from one site to adjacent vacant site contributes to the dc conductivity[63]. In the high frequency dispersive region, the behaviour of conductivity can be assigned to the charge carriers transfer between various ions and release of charges from different confined centers due to the electric force of applied changing electric field. Increase in frequency, results in an increase in mobility of the charge carriers, which in turn, results into increase in conductivity of the material.

The conductivity data so obtained can be fitted by using the Jonscher's power law, the equation of which can be represented as $\sigma_{total}(\omega,T) = \sigma_{dc}(T) + A(T)\omega^s$ [64], where, σ_{total} is the total conductivity of the sample, which is equal to the sum of dc and ac conductivity, σ_{dc} is the dc conductivity, the term $A(T)\omega^s$ indicates ac conductivity. The temperature dependent term $A(T)$, which determines the strength of polarizability[65] has a unit of conductivity and s is a power law exponent, which depends on temperature and composition of the sample and varies between 0 and 1[52]. It represents the degree of interaction between mobile ions with lattice.

Figure 9 shows highly dispersive behavior for the synthesized sample due to the existence of ac conductivity. The values of power-law exponent '*s*' and factor '*A*' are calculated from the slope and intercept of the plot of Fig. 9 and obtained 0.507 and 7.33×10^{-8} S m^{-1} rad^{-n}, respectively. The value of exponent '*s*' determines the type of conduction mechanism. The zero value of '*s*', *i.e.*, $s = 0$ indicates frequency-independent or dc conduction, while $s \leq 1$ indicates frequency-dependent or ac conduction due to the translational motion of the charge carriers with a sudden hopping[66,67]. Further, the value of exponent

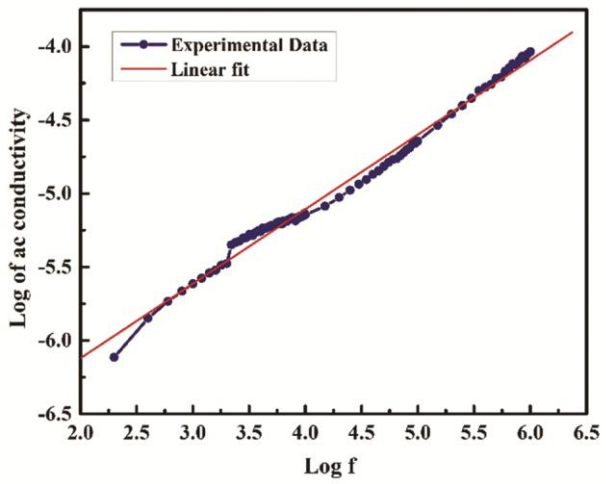

Fig. 9 — Johnscher plot.

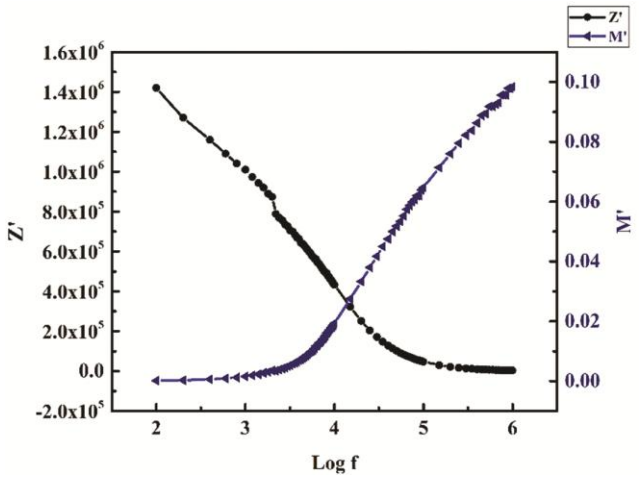

Fig. 10 — Frequency dependence of Z' and M'.

'*s*' between 0.5 and 1 indicates ideal long-range pathways and diffusion-limited hopping[68]. In the present case, the value of '*s*' indicates frequency-dependent conduction due to the ideal long-range and diffusion-limited hopping of charges.

3.4.2 Spectroscopic impedance and modulus analysis

Complex impedance and modulus spectroscopic techniques are very powerful tools to understand the behavior of a polycrystalline material. These analyses can be utilized to identify the grain and /or grain boundary contributions in such materials, as the characteristics of both are different from each other. These techniques hold four elementary formalisms namely, permittivity, impedance, modulus and admittance, to find out the possible confirmation concerning the electrical characteristics of the material. These are non-destructive techniques to find out the electrical properties of the material over a wide range of temperature as well as frequency ranges. In the present investigation, to differentiate between the electrode, grain and/or grain boundary response of and to identify the dominancy of grain and/or grain boundary contribution in the synthesized material, the impedance measurement has been carried out in a wide range of frequency (100 Hz to 1 MHz) at room temperature.

Frequency dependence of Z' and M'

Figure 10 shows frequency dependence of real (Z') and real (M') components of complex impedance and complex modulus, respectively.

It is observed from the plot of Fig. 10 that the value of Z' decreases with an increase in frequency. This indicates an increase in ac conductivity of the sample with the increase in frequency[69] and the presence of space charge polarization within this region of frequency because the space charge has enough time to relax within this region of frequency. Further, the higher value of Z' can be attributed to the enhanced hopping of charge carriers between the localized ions[70]. This also indicates that both capacitive and resistive components are dynamic in this range of frequency[71]. At higher frequencies, the Z' achieves a very low constant value and becomes almost independent of frequency. This can be attributed to the inability of space charges to follow the high-frequency fields[72,73] because of having lesser time to relax at higher frequency region, resulting in fast recombination and hence, reduction in the space charge polarization[74].

The observation of *M'* versus *logf* plot of Fig. 10 shows that in the beginning, the value of *M'* is very close to zero, which indicates the elimination electrode polarization[75,76]. Then as the frequency increases, an increase in the value of M' is observed, which indicates that the relaxation processes over the range of frequencies within which the value of M' increases with frequency are distributed[77]. Generally, the dispersion in the value of M' with frequency is followed by a peak in the plot of M'' versus *logf*, discussed in the very next section and the ability of the charge carriers to move freely over a short range under the presence of electric field. The M' plot shows dispersion not a peak, which may be due the equivalency of M' in complex electric modulus with ε' in complex permittivity[78].

Frequency dependence of Z" and M"

Figure 11 shows frequency dependence of imaginary (Z'') and imaginary (M'') components of

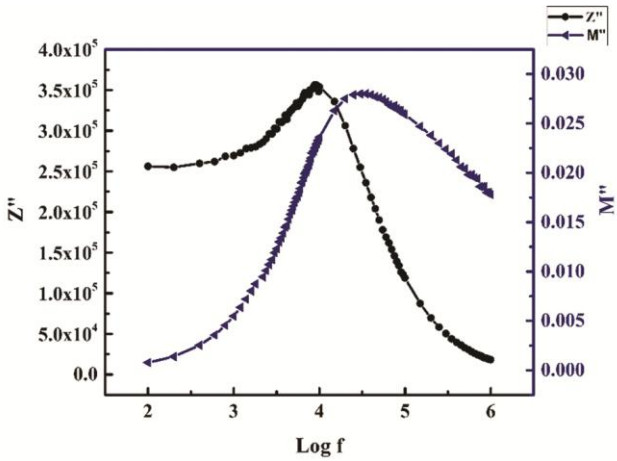

Fig. 11 — Frequency dependence of Z'' and M''.

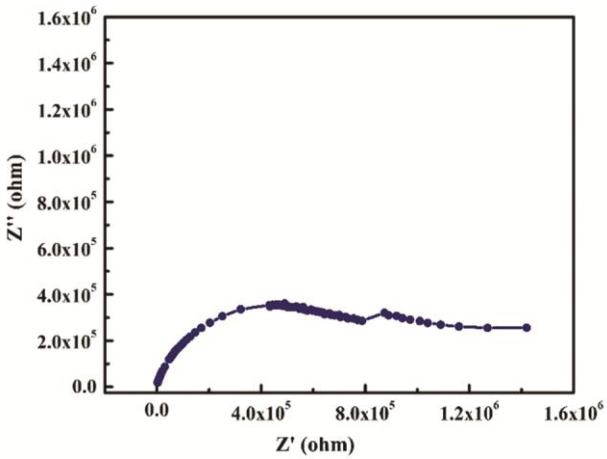

Fig. 12 — Nyquist plot.

complex impedance and complex modulus, respectively.

It is noticed from the plot that the value of *Z″* attains a maximum value at a certain frequency called the relaxation frequency and then as the frequency increases, the value of *Z″* decreases. The presence of a single relaxation peak can be attributed to the relaxation process in the material due to the presence of electrons/immobile species. The peak height is proportional to bulk/grain resistance (R_b) and can be estimated by the equation $Z'' = R_g\{\omega\tau/(1+\omega^2\tau^2)\}$ in *Z″* versus frequency plot[79]. Further, the trend of the plot shows frequency-independent behavior of *Z″* at high frequencies, which may be attributed to the release of space charge in the sample[80-82].

From the plot of *M″* versus *logf*, it is observed that the value of *M″* is quite low for the initial frequency of measurement, which can be attributed to the absence of electrode polarization phenomena[83]. Then, as the frequency increases the plot exhibits a single and broad relaxation peak with the absence of any other peaks visible in the frequency range investigated, implying that the synthesized material represents grain effect only[84,85]. The region on the left of the peak determines the range in which charge carriers are mobile over long distances, which means performing successful hopping from one site to the neighboring site whereas the region to the right is the region where carriers are confined to potential wells being mobile over short distances or can execute only localized motion[76,77,86,87]. The asymmetric broadening as well as non-overlapped of the relaxation peaks, suggest a spread of relaxation time and non-Debye type of relaxation in the material[83,88].

β parameter

In order to investigate the percentage of deviation with respect to Debye type relaxation, the exponent parameter β has been calculated by using the equation $\beta = \frac{1.14}{FWHM}$[78,89]. Here, FWHM is the full width at half maximum of *M″* versus *logf* curve and obtained from Gaussian type curve fitting. The highest value of exponent parameter *β*, *i.e.*, $\beta = 1$ indicates Debye type and ideal dielectric relaxation, while smaller the value of *β* shows higher is the deviation of relaxation with respect to Debye type relaxation indicating considerable dipole-dipole interaction in the case of the real system[88]. In the present case, the obtained value of *β* is 0.48, indicating a greater deviation of relaxation with respect to Debye type relaxation. Further, this parameter can be interpreted as a result of connected motions between the ions[90]. The smaller value of *β* parameter indicates more extended participation between the charge carriers. In the present case, the obtained value of *β* nearly 0.5, can be interpreted as an extended coupling between the charge carriers, resulting in a good concentration of mobile ions within the sample.

3.4.3 Nyquist plot analysis

From the Nyquist plot, various electrical parameters such as the values of grain/bulk resistance and corresponding capacitance, grain-boundary resistance and corresponding capacitance, constant phase element (CPE) factor (in case of non-ideal capacitive behavior of the circuit) and frequency power '*n*' can be evaluated with the help of the software Z-view. The frequency-dependent real component of impedance (*Z′*) versus imaginary component (*Z″*) curve, known as the Nyquist plot[91,92] at room temperature within the frequency range 100 Hz to 1MHz is shown in Fig. 12.

The trend of the curve shows a bending towards the real, *i.e.*, *Z'* axis and takes the shape of a semicircle. It is worth to mention here that the formation of full, partial or no semicircle depends on the strength of relaxation and available frequency range[83,93]. Moving towards origin from the left, the frequency of the applied field increases and hence, it can be observed from the plot that the high-frequency arc passes through the origin. The center of the semi-circular arc lies below the real axis, that is, a depressed semicircle is observed, which confirms the existence of a non-Debye type of relaxation in the sample. Depending upon the electrical properties of the material, one, two or more semi-circular arcs may be obtained from the impedance plot. Moving towards right from the origin, the first semicircle at high frequency and second semicircle at low frequency can be assigned to grain/bulk resistance and grain-boundary resistance, respectively[94-96]. In the present case, while fitting the experimental data by using the software Z-view, a single semi-circle throughout the complete impedance plane is observed, suggesting the major contribution from the grain to the conduction mechanism in the sample. When such semi-circle customized in terms of an equivalent electrical circuit, result into parallel RC circuit. If capacitor is not an ideal capacitor, then semi-circle can be customized into parallel R-CPE, i.e., constant phase element circuit. In the present case, the fitting of the semi-circle results into parallel R-CPE circuit as shown in the Fig. 13.

The value of capacitance is calculated by using the equation $C = \left[R^{(1-\alpha)}.Q^{1/\alpha}\right]$[97]. Here, α is the degree of deviation with respect to the value of the pure capacitor. Its value is unity for the pure capacitor and is zero for the pure resistor. As only grain effect is dominant in the sample within the frequency range studied, *R* represents the grain resistance, the value of which can be obtained from the intercept of each semicircle with the real axis. The relaxation time for grain is calculated by using the relation $\tau_g = R_g \cdot C_g$. The value of α_g shows the degree of deviation for grain. All the equivalent circuit parameter values are listed in Table 6.

To recognize the relaxation process present within the sample clearly, a Bode plot shown in Fig. 14 is taken into account. The plot shows the dependence of the phase of the impedance on frequency. At lower frequencies and higher frequencies, the observed shapes confirm the presence of grain only and relaxation mechanism expressed by the equivalent R-CPE circuit[85].

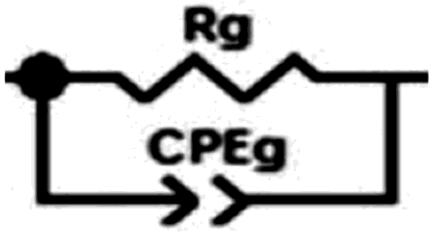

Fig. 13 — R-CPE equivalent circuit.

3.4.4 Cole-cole plot analysis

The frequency-dependent real component of modulus (*M'*) versus imaginary component (*M''*) curves, known as the Cole-Cole plot[92,93] at room temperature within the frequency range 100 Hz to 1MHz is shown in Fig. 15.

Table 6 — Equivalent circuit parameters

Ferrite composition	R_g (MΩ)	C_g (pF)	τ_g (ms)	α_g
$Mn_{0.6}Co_{0.2}Ni_{0.2}Fe_2O_4$	0.932	18.64	0.0174	0.819

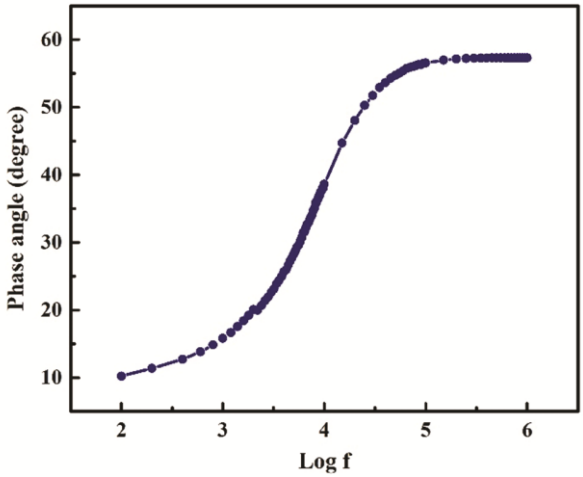

Fig. 14 — Bode plot.

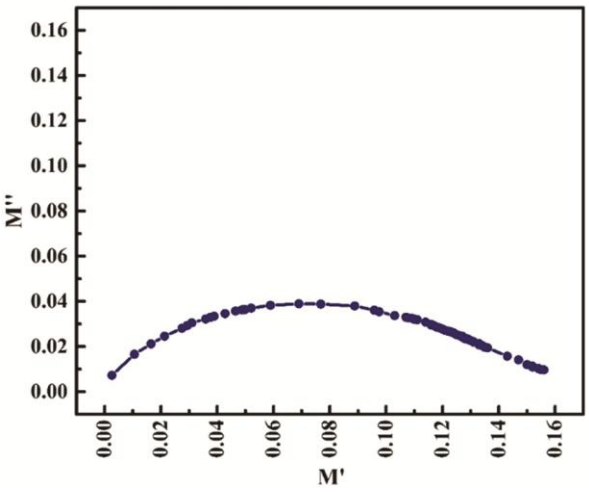

Fig. 15 — Cole-Cole plot.

The plot clearly shows a single semicircle, which indicates the presence of grain contribution in the sample. The center of the semicircle does not lie on the real axis indicating non-Debye type relaxation within the sample and spread of relaxation. Hence, in spite of the Nyquist plot, the Cole-Cole plot helps to sort out the relaxation process in a clear manner.

4 Conclusion

Ternary nano-structured ferrite $Mn_{0.6}Co_{0.2}Ni_{0.2}Fe_2O_4$ was successfully synthesized by the citrate-gel auto-combustion technique. The elemental stoichiometry was confirmed by EDAX analysis. The cubic spinel structure belonging to the *Fd3m* space group was confirmed by X-ray diffraction. The structural parameters like crystallite size, porosity, surface area, ionic and site radii, hoping length, oxygen positional parameters, shared and unshared edge length were evaluated through the XRD analysis. According to Waldron's classification, the absorption bands v_1 and v_2 were found around 600 cm^{-1} and 400 cm^{-1}, which confirmed the basic characteristic of spinel ferrite. The value of dielectric constant and dielectric loss decreased as the frequency increased suggested the basic nature of spinel ferrites. The Johnscher plot indicated the frequency-dependent conduction. Frequency-dependent impedance and modulus analysis suggested a non-Debye type of relaxation in the sample. From the Nyquist plot analysis single semi-circular arc is observed which confirmed the conduction in the sample is only because of the grains present in the ferrite sample which is modeled using a parallel R-CPE circuit. The Cole-Cole plot showed a single semicircle which confirmed the presence of only grains in the contribution of the conduction mechanism in the sample.

Acknowledgement

One of the authors (LJH) is thankful to University Grants Commission, New Delhi for providing a research fellowship.

References

1 Petrova E, Kotsikau D & Pankov V, *J Magn Mag Mater*, 378 (2015) 429.
2 Hcini S, Selmi A, Rahmouni H, *et al. Ceram Inter*, 43 (2017) 2529.
3 Kombaiah K, Vijaya J J, Kennedy L J, *et al. Optik*, 135 (2017) 190.
4 Sharma R, Thakur P, Kumar M, *et al*. *J Alloys Compd*, 684 (2016) 569.
5 Desai H B, Hathiya L J, Joshi H H & Tanna A R, *Mater Today Proc*, 21 (2020) 1905.
6 Sharma R P, Raut S D, Kadam A S, *et al*., *Appl Phys A*, 126 (2020) 824.
7 Bhatu S S, Lakhani V K & Tanna A R, *Indian J Pure Appl Phys*, 45 (2007) 596.
8 Singh N, Aggarwal A, Sanghi S & Khasa S, *J Magn Magn Mater*, 324 (2012) 2506.
9 Fatemi D J, Harris V G, Chen M X, *et al. J Appl Phys*, 85 (1999) 5172.
10 Rana G, Johri U C & Asokan K, *EPL*, 103 (2013) 17008.
11 Bhandare S V, Kumar R, Anupama A V, *et al. J Magn Magn Mater*, 433 (2017) 29.
12 Wang G, Zhao D, Kou F, *et al*., *Chem Eng J*, 351 (2018) 747.
13 Bellini J V, Medeiros S N, Ponzoni A L & Longen F R, *Mater Chem Phys*, 105 (2007) 92.
14 Deraz N M & Shaban S, *J Anal Appl Pyro*, 86 (2009) 173.
15 Chand P, Vaish S & Kumar P, *Phys B*, 524 (2017) 53.
16 Raouf A H, Emamian H R, Yourdkhani A & Ataie A, *Int J Mod Phys B*, 24 (2010) 5807.
17 Song Q & Zhang Z J, *J Am Chem Soc*, 126 (2004) 6164.
18 Bansal M, Aghamkar P & Ahlawat D S, *Int J Serv Tech Manag*, 4 (2015) 871.
19 Melinon P, Colin S B, Duvail J L, *et al*., *Phys Rep*, 543 (2014) 163.
20 Nejati K & Zabihi R, *Chem Cent J*, 6 (2012) 23.
21 Genc F, Unal B, Baykal A & Sozeri H, *J Super Nov Magn*, 28 (2015) 1055.
22 Reddy C V, Manorama S V & Rao V J, *Sens Actu B*, 55 (1990) 90.
23 Sivakumar N, Narayanasamy A & Ponpandianb N, *J Appl Phys*, 101 (2007) 084116.
24 Vestal C R & Zhang J Z, *Int J Nanotech*, 1 (2004) 240.
25 Alarifi A, Deraz N M & Shaban S, *J Alloys Compd*, 486 (2009) 501.
26 Cullity B D & Graham C D, Introduction to magnetic materials (John Wiley & Sons), 2009.
27 Junaid M, Khan M A, Akhtar M N, *et al*., *Ceram Inter*, 45 (2019) 13431.
28 Patil K C, Aruna S T & Mimani T, *Current Opin in Sol State & Mater Sci*, 6 (2002) 507.
29 Hajalilou A & Mazlan S A, *Appl Phys A*, 122 (2016) 680.
30 Chaibakhsh N & Shoeili Z M, *Mater Sci Eng C*, 99 (2019) 1424.
31 Kefeni K K, Msagati T A & Mamba B B, *Mater Sci Eng B*, 215 (2017) 37.
32 Hathiya L J, Tanna A R, Baraliya J D & Joshi H H, *AIP Conf Proc*, 2220 (2020) 020155.
33 Hathiya L J, Baraliya J D, Das A, *et al*., *Indian J Phys*, (2021), in press.
34 Farooq H, Ahmad M R, Jamil Y, *et al*., *J Basic Appl Sci*, 8 (2012) 597.
35 Satalkar M & Kane S N, *J Phys Conf Ser*, 755 (2016) 012050.
36 Ohnishi H & Teranishi T, *J Phys Soc Jpn*, 16 (1961) 36.
37 Tanna A R & Joshi H H, *World Acad of Sci Eng Tech*, 75 (2013) 334.
38 Miller A, *J Appl Phys*, 30 (1959) 245.
39 Culity B D, Elements of X-Ray Diffraction (Addison Wesely publishing company Inc), 1959, p. 132.
40 Modi K B, Gajera J D, Chhantbar M C, *et al*., *Mater Lett*, 57 (2003) 4049.

41 Globus A, Pascard H & Cagan V, *J Phys Suppl*, 438 (1977) 439.
42 Mazen S A, Abdallah M H, Sabrah B A & Hasham H A, *Phys Stat Solidi A*, 134 (1992) 263.
43 Prasad B B, Ramesh K V & Srinivas A, *Mater Sci-Pol*, 37 (2019) 39.
44 Waldron R D, *Phys Rev B*, 99 (1955) 1727.
45 Ravinder D, *Mater Lett*, 40 (1999) 198.
46 Naik M M, Naik H S, Nagaraju G, *et al*., *J Mater Sci: Mater Electron*, 29 (2018) 20395.
47 Xiao S H, Jiang W F, Li LY & Li X J, *Mater Chem Phys*, 106 (2007) 82.
48 Reddy C V, Vattikuti S V, Ravikumar R V et al. *J Magn Magn Mater*, 394 (2015) 70.
49 Nasrin S, Khan S M, Matin M A, *et al*., *J Mater Sci: Mater Electron*, 30 (2019) 10722.
50 Meiorin C, Muraca D, Pirota K R, *et al*., *Eur Polym J*, 53 (2014) 90.
51 Whike W B & Angelis B A, *Spectro Acta*, 23A (1967) 985.
52 Bhat B H, Samad R & Want B, *Appl Phys A*, 122 (2016) 810.
53 Kumar N, Shukla A, Kumar N & Choudhary R N, *J Mater Sci: Mater Electron*, (2021), in press.
54 Maxwell J C, Electricity & Magnetism (Oxford Uni. Press, London), 1973.
55 Wagner K W & Heilman E L, *Ann Phys*, 40 (1993) 818.
56 Koops C G, *Phys Rev*, 83 (1951) 121.
57 Soman V V, Nanoti V M & Kulkarni D K, *Ceram Inter*, 39 (2013) 5713.
58 Mondal R A, Murty B S & Murthy V R, *J Alloys Compd*, 595 (2014) 206.
59 Kanamadi C M & Chougule B K, *Mater Chem Phys*, 93 (2005) 548.
60 Tripathi R, Kumar A & Sinha T P, *Praman J. Phys*, 72 (2009) 969.
61 Lee W K, Lim B S, Liu J F & Nowick A S, *Sol State Ion*, 831 (1992) 53.
62 Dutta A, Bharti C & Sinha T P, *Indian J Eng Mater Sci*, 15 (2008) 181.
63 Gohel K & Kanchan D K, *J Adv Dielec*, 8 (2018) 185005.
64 Jonscher A K, *Nature* 256 (1977) 673.
65 Karthik C & Varma K B, *J Phys Chem Solids*, 67 (2006) 2437.
66 Batoo K M, *Phys B*, 406 (2011) 382.
67 Funke K, *Prog Sol State Chem*, 22 (1993) 111.
68 Mauritz K A, *Macromolecules*, 22 (1989) 4483.
69 Saif A A, Jamal Z A, Sauli Z & Poopalan P, *Mater Sci Medzg*, 17 (2011) 186.
70 Srinivasamurthy K M, Manjunatha K, Sitalo E I, *et al*., *Indian J Phys*, 94 (2020) 593.
71 Saif A A & Poopalan P, *J Korean Soc*, 57 (2010) 1449.
72 Plocharski J & Wieczoreck W, *Sol State Ion*, 979 (1988) 28.
73 Ganguly P & Jha A K, *Bull Mater Sci*, 34(4) (2011) 907.
74 Anupama M K, Rudraswamy B & Dhananjaya N, *J Alloys Comp*, 706 (2017) 554.
75 Yakuphanoglu F, *Phys B*, 393 (2007) 139.
76 Dutta A, Sinha T P, Jena P & Adak S, *J Non-Cryst Solids*, 354 (2008) 3952.
77 Patro L N & Hariharan K, *Mater Chem Phys*, 116 (2009) 81.
78 Aziz S B, Abidin Z H & Arof A K, *Exp Poly Lett*, 4 (2010) 300.
79 Das P R, Pati B, Sutar B C & Choudhury R N, *J Mod Phys*, 3 (2012) 870.
80 Pradhan D K, Choudhary R N, Rinaldi C & Katiyar R S, *J Appl Phys*, 106 (2009) 102.
81 Haun M J, Furman E, Jang S J & Cross L E, *Ferroelectrics*, 99 (1989) 13.
82 Grinberg I, Cooper V R & Rappe A M, *Phys Rev* B, 69 (2004) 144118.
83 Ranjan R, Kumar N, Behera B & Choudhary R N, *Adv Mat Lett*, 5 (2014) 138.
84 Ahmadu U, Tomas S, Jonah S A, *et al*., *Adv Mat Lett*, 4 (2013) 185.
85 Joshi J H, Joshi G M, Joshi M J, *et al*., *New J Chem*, 42 (2018) 17227.
86 Kim J S, *J Phys Soc*, 70 (2001) 3129.
87 Rawat A, Mahavar H K, Tanwar A & Singh P J, *Bull Mater Sci*, 37 (2014) 273.
88 Joshi J H, Kalainathan S, Kanchan D K, *et al*., *J Mater Sci: Mater Electron*, 30 (2019) 2985.
89 Jonge J J, Zon A V & Leeuw S W, *Sol State Ion*, 147 (2002) 349.
90 Dasari M P, Rao K S, Krishna P M & Krishna G G, *Acta Phys Polon A*, 119 (2011) 387.
91 Thansanga L, Shukla A, Kumar N & Choudhary R N, *Phase Trans*, 94 (2021) 47.
92 Acharya P G, Behera S, Choudhary R N & Parida S K, *J Mater Sci: Mater Electron*, (2021), in press.
93 Garhardt R J, *Phys Chem Solids*, 55 (1994) 1491.
94 Want B, Bhat B H & Ahmad B Z, *J Alloys Compd*, 627 (2015) 78.
95 Pattanayak R, Panigrahi S, Dash T, *et al*., *Phys B*, 474 (2015) 57.
96 Kotnala R K, Dar M A, Verma V & Siddiqui W A, *J Magn Magn Mater*, 322 (2010) 3714
97 Joshi J H, Kanchan D K, Joshi M J, *et al*., *Mater Res Bull*, 93 (2017) 63.